



Contents lists available at ScienceDirect

Journal of the Mechanics and Physics of Solids

journal homepage: [www.elsevier.com/locate/jmps](http://www.elsevier.com/locate/jmps)

# A theoretical-numerical model for the peeling of elastic membranes <sup>☆,☆☆</sup>

Daniele Liprandi <sup>a</sup>, Federico Bosia <sup>b</sup>, Nicola M. Pugno <sup>a,c,d,\*</sup>

<sup>a</sup>Laboratory of Bio-Inspired and Graphene Nanomechanics, Department of Civil, Environmental and Mechanical Engineering, University of Trento, Via Mesiano 77, I-38123 Trento, Italy

<sup>b</sup>Department of Physics and Nanostructured Interfaces and Surfaces Interdepartmental Centre, Università di Torino, Via P. Giuria 1, 10125 Torino, Italy

<sup>c</sup>School of Engineering and Materials Science, Queen Mary University, Mile End Rd, London E1 4NS, UK

<sup>d</sup>KET Labs, Edoardo Amaldi Foundation, Via del Politecnico snc, 00133 Rome, Italy

## ARTICLE INFO

### Article history:

Received 25 May 2019

Revised 25 August 2019

Accepted 14 September 2019

Available online xxx

## ABSTRACT

The adhesive behavior of biological attachment structures such as spider web anchorages is usually studied using single or multiple peeling models involving “tapes”, i.e. one-dimensional contacts elements. This is an oversimplification for many practical problems, since the actual delamination process requires the modeling of complex two-dimensional adhesive elements. To achieve this, we develop a theoretical-numerical approach to simulate the detachment of an elastic membrane of finite size from a substrate, using a 3D cohesive law. The model is validated using existing analytical results for simple geometries, and then applied in a series of parametric studies. Results show how the pull-off force can be tuned or optimized by varying different geometrical or mechanical parameters in various loading scenarios. The length of the detachment boundary, known as the peeling line, emerges as the key factor to maximize adhesion. The approach presented here can allow a better understanding of the mechanical behavior of biological adhesives with complex geometries or with material anisotropies, highlighting the interaction between the stress distributions at the interface and in the membrane itself.

© 2019 Elsevier Ltd. All rights reserved.

## 1. Introduction

Adhesion is a topic that has attracted great interest in the mechanics community in recent years. The field of biological materials has allowed to exploit theories for adhesion formulated in the past (Kendall, 1975; Maugis, 1992; Palacio and Bhushan, 2012) and has stimulated the formulation of novel theories and models for complex problems emerging from bio-mimetics (Lai et al., 2009; Carbone et al., 2011; Prokopovich and Starov, 2011; Brodoceanu et al., 2016; Cutkosky, 2015), from bio-mechanics (Arzt et al., 2003; Tian et al., 2006; Grawe et al., 2014; Labonte and Federle, 2016) or even from nano-mechanics (Rakshit and Sivasankar, 2014; Mo et al., 2015). Biological adhesives have been studied in depth for the optimization process they have undergone in the course of thousands of years of evolution (Chen et al., 2009; Pugno and Lepore, 2008; Wolff and Gorb, 2016). The term “smart adhesion” has been introduced to describe the amazing adhesive

<sup>☆</sup> 60<sup>th</sup> Anniversary Issue of JMPS in Honour of Davide Bigoni.

<sup>☆☆</sup> This paper was submitted, reviewed and accepted as a normal paper for JMPS and was transferred to this Special Issue after acceptance.

\* Corresponding author.

E-mail address: [nicola.pugno@unitn.it](mailto:nicola.pugno@unitn.it) (N.M. Pugno).

properties common to different species of animals and plants (Bhushan, 2007), which have been a source of inspiration for adhesive elements and manipulators in robotics (Kim et al., 2008; Daltorio et al., 2005). Frictional properties of adhesive systems have also been recently discussed (Shen et al., 2009; Das et al., 2015; Tian et al., 2006), and progress has been made in tribology to investigate the behavior observed at the small scale, leading to new adhesion, adhesion-friction and adhesion-wear models (Leonard et al., 2012; Brely et al., 2018a; Vakis et al., 2018). This is often achieved by modeling the interface between the body and the substrate using elements governed by a traction-displacement law (Dimaki et al., 2016). This feature is the basis of Cohesive Zone Models (CZM) (Barenblatt, 1962; Xu and Needleman, 1994; Dimitri et al., 2015; Park and Paulino, 2013), which have also been recently used to analyze the interaction between adhesion and friction (Salehani et al., 2018).

In the literature, adhesive problems are mainly described by referring to two configurations: contact mode and peeling mode, which are based on the Johnson-Kendall-Roberts (Johnson et al., 1971) or Derjaguin-Muller-Toporov (Derjaguin et al., 1975) theories, and on the Kendall single peeling theory (Kendall, 1975), respectively. The considered geometries exploit symmetries to derive 1D or 2D solutions. Recent works have shown how the Boundary Element Method can be used to numerically solve adhesive problems for an arbitrarily-shaped contact areas between an elastic half-space and a rigid indenter (Pohrt and Popov, 2015; Rey et al., 2017). However, these models only treat normal contact problems, where the indenter is applied vertically, and thus the adhesive directionality of the membrane is not analyzed. In general, the problem of describing how an elastic membrane of finite size adheres, deforms and delaminates from an adhesive surface remains to be fully addressed. The solution of this problem is of interest both for fundamental mechanics and biology, as well as for applications in areas like the biomedical or packaging sectors.

In this paper, we propose a three-dimensional approach which combines a lattice model (Ostoja-Starzewski, 2002; Chen et al., 2014) and a CZM to describe the adhesive properties of elastic membranes. To our knowledge, this is the first attempt to model the peeling of finite-sized thin films or membranes. This approach provides a number of advantages with respect to standard Finite Element Methods (FEM), aside from straight forward implementation and improved computational times: the possibility of simulating adhesion of thin films on soft, finite thickness substrates, which is usually extremely challenging using FEM approaches (Crocconbe and Adams, 1981; Thouless and Yang, 2008; Yastrebov et al., 2011; Sauer, 2016); the possibility of direct implementation of non-linear analysis using the same reticular structure and standard solution algorithms; the additional possibility of easily capturing phenomena such as wrinkling and fracture (Cerdeja and Mahadevan, 2003; Brely et al., 2015). These characteristics are discussed in the paper, and solutions are sought for varying geometries, loading conditions and membrane properties, including anisotropy, so as to include as subcases known results in the literature, such as tape single peeling and axisymmetric membrane peeling.

## 2. Model

### 2.1. Interface

Delamination processes are often simulated using CZM. These are based on traction-separation laws, i.e. cohesive laws, which simulate the behavior of an adhesive interface (Dugdale, 1960; Park and Paulino, 2013; Barenblatt, 1962). It was shown (Savkoor and Briggs, 1977; Warrior et al., 2003; McGarry et al., 2014) that in adhesive contact problems, detachment occurs in a mixed-mode configuration and a coupled cohesive law is necessary, in which the traction along the  $i$  th direction for every single node of the membrane depends upon its displacement along all three direction components. Despite the extensive literature on the subject, most cohesive laws are two-dimensional (2D) and only a few works deal with 3D cohesive zones. A widespread practice is to avoid a complete definition of a 3D cohesive law by using an effective gap value

$$\Delta_{eff} = \sqrt{\Delta_z^2 + \beta^2 \Delta_x^2 + \beta^2 \Delta_y^2} \quad (1)$$

where the fracture propagation line is assumed to belong to the  $xy$  plane and  $\beta$  is a scalar value used to assign different weights to the normal gap  $\Delta_z$  and the tangential gaps  $\Delta_x$  and  $\Delta_y$ . The effective gap  $\Delta_{eff}$  can be used in a 1D traction-displacement law, supplying a straightforward 3D formulation. However, there is no proof that a correct coupling and realistic results are obtained with this approach. In other works, 3D complete models were formulated for various applications like the adhesion of carbon nanotubes (Hu, 2010), fracture propagation in graded materials (Zhang and Paulino, 2005) or indentation problems (Salehani and Irani, 2018).

In this work, we use a simplified version of 3D coupled cohesive laws found in previous literature. This formulation is based on the normal components of the general potential-based models (Rice and Wang, 1989; McGarry et al., 2014). The adopted traction-displacement ( $T_m$ ,  $\Delta_m$ ) relationship is

$$T_m = \Delta_m \frac{\phi_m}{\delta_m^2} \cdot \exp \left( \sum_n - \frac{\Delta_n^2}{\delta_n^2} \right) \quad (2)$$

where  $\phi_m$ ,  $\Delta_m$  and  $\delta_m$  are the work of separation, the crack gap value and the characteristic length (i.e. the gap value corresponding to the maximum traction), respectively, in the direction  $m$ , and  $m$  and  $n$  are the direction indexes that can assume the values  $\{x, y, z\}$ . The energy per unit area  $\Delta\gamma_m$  can be defined as  $\Delta\gamma_m = \phi_m/A$ , where  $A$  is the contact

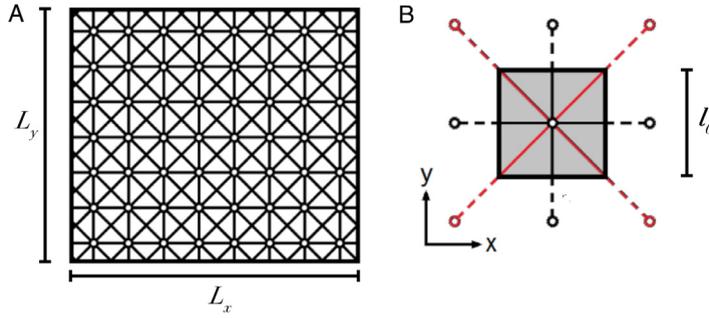


**Fig. 1.** Membrane discretization: (A) Example of a grid made of x-braced squared elements: (B) Elementary cell. Every node is connected by a truss element to its nearest neighbours (black lines) and next-nearest neighbours (red lines).

area. If the work of separation and the characteristic length are the same for the normal and tangential directions, Eq. (2) becomes

$$T_m = \Delta_m \frac{\phi}{\delta^2} \cdot \exp\left(\frac{-\Delta_{eff}^2}{\delta^2}\right) \tag{3}$$

where Eq. (1) with  $\beta = 1$  is used to define  $\Delta_{eff}$ . The interface stress  $\sigma_i$  can now be defined as

$$\sigma_i = \text{sqr}t\left(\sum_m T_{2m}\right) / A \tag{4}$$

The simplified cohesive law in Eq. (3) is based on several assumptions: that the traction and compression behavior is the same, that there is reversibility (this is not the case when damage is present, since the loading and unloading phases are different) and that there is a softening region. Although Eq. (3) is not suitable to treat mechanical problems where large compressive values occur, the aim of this work is to calculate crack openings where there is little or no compression. This condition should be verified by comparing numerical results with analytical equations.

### 2.2. Theoretical model

To numerically model a continuous body like an elastic membrane, it is important to choose an appropriate discretization criterion. One of the possible approaches is to describe the structure as a grid of points in 3D space connected by 1D bonds forming a network. This approach, first denominated framework method (Hrennikoff, 1941), was introduced in the first half of the past century and has led to the development of numerous discretized models used today (Nukala et al., 2005; Ostoja-Starzewski, 2002; Brely et al., 2015; Costagliola et al., 2018), thanks to its computational advantages. By varying the mechanical properties attributed to the elements, the anisotropic behavior of heterogeneous materials can be studied. The procedure described in (Valoroso and Champany, 2006; Zhang and Paulino, 2005) is used to build a grid of x-braced elements (Fig. 1) to discretize the membrane, which is considered homogenous and linear elastic, with a Poisson's ratio of  $\nu = 1/3$ , as imposed by plane stress conditions and mesh definition. The determination of the geometrical and physical parameters in order to obtain equivalence with an elastic continuum is based on the equivalence between the strain energy  $U_{cell}$  stored in the discretized unit cell and the strain energy  $U_{cont}$  stored in a continuous membrane of the same volume (Absi and Prager, 1975), written as:

$$U_{cell} = \frac{1}{2} \sum_k A_k \sigma(\varepsilon_k) \varepsilon_k \tag{5}$$

$$U_{cont} = \frac{1}{2} \int_V \sigma_{cont}(\varepsilon) \varepsilon dV \tag{6}$$

The discrete cell must have the same linear elastic behavior as the membrane, i.e.:

$$\sigma(\varepsilon_k) = E \cdot \varepsilon_k \tag{7}$$

where  $E$  is the Young's modulus of both the membrane and the truss elements. By substituting Eq. (7) in Eqs. (5) and (6) and imposing the equivalence between the strain energies, it is found that

$$A_d = \frac{3\sqrt{2}}{8} lt \tag{8}$$

$$A_l = \frac{3}{8} lt \tag{9}$$

where  $A_l$  is the cross-section of the orthogonal springs,  $A_d$  is the cross-section of the diagonal springs and  $t$  is the thickness of the continuous membrane. Other Poisson's ratios can be obtained by introducing 3-node links and other types of meshes (Ostoja-Starzewski, 2002).

Once the set of points and bonds is defined, a mathematical formulation for the equilibrium equations is needed. The formulation must take into account the geometrical non-linearities that can appear for large displacements. In this work, a generalized 3D co-rotational truss formulation is used (Yaw, 2009; Limkatanyu et al., 2013; Nishino et al., 1984), i.e. the bonds sustain axial loads only. Given a set of  $N$  points  $x_i = (x, y, z)$  connected by a grid of  $S$  springs, the truss  $k$  is defined by its two end points with indexes  $p$  and  $q$ , its cross-section  $A$ , its initial length  $l_0$ , its current length  $l$ , and by the constitutive non-linear elastic stress-strain equation  $\sigma = \sigma(\varepsilon)$ . The axial force in a single truss member is  $N(\varepsilon) = A \cdot \sigma(\varepsilon)$ . The internal force vector  $\mathbf{Q}_i$  is derived by computing the derivative of the elastic potential energy  $U$  with respect to the global displacement vector  $\mathbf{u}$ :

$$\mathbf{Q}_i = \frac{\partial}{\partial \mathbf{u}} U \quad (10)$$

The derivative can be rewritten using the chain rule, obtaining:

$$\frac{\partial}{\partial \mathbf{u}} = \frac{\partial}{\partial(\Delta l)} \frac{\partial(\Delta l)}{\partial \mathbf{u}} \quad (11)$$

where  $\Delta l = l - l_0 = \varepsilon l_0$  is the axial displacement. The second term of this differential is given by the element cosines in the 3D space, which are:

$$n_1 = \frac{x_p - x_q}{l} \quad n_2 = \frac{y_p - y_q}{l} \quad n_3 = \frac{z_p - z_q}{l} \quad (12)$$

The tangent stiffness matrix  $\mathbf{K}$ , used to linearize the set of equations describing the problem, is defined as

$$\mathbf{K} = \frac{\partial}{\partial \mathbf{u}} \mathbf{Q}_i = \frac{\partial^2}{\partial \mathbf{u}^2} U = \frac{\partial}{\partial \mathbf{u}} \left( A \sigma(\varepsilon) \frac{\partial(\Delta l)}{\partial \mathbf{u}} \right) = A \frac{\partial \sigma}{\partial \varepsilon} \frac{\partial(\Delta l)}{\partial \mathbf{u}} + A \sigma \frac{\partial^2(\Delta l)}{\partial \mathbf{u}^2} \quad (13)$$

Following (Yaw, 2009), the two terms are indicated respectively as the material and the geometric stiffness matrixes ( $\mathbf{K}_m$  and  $\mathbf{K}_g$ ). Defining the transformation vector as

$$\mathbf{n} = [n_1 \quad n_2 \quad n_3 \quad -n_1 \quad -n_2 \quad -n_3] \quad (14)$$

the two matrices can be written in the global coordinate system as

$$\mathbf{K}_m = A_k \frac{\partial \sigma}{\partial \varepsilon_k} \cdot \mathbf{n}^T \mathbf{n} \quad (15)$$

$$\mathbf{K}_g = \frac{N_k(\varepsilon_k)}{l_k} \begin{bmatrix} \mathbf{I}_3 & -\mathbf{I}_3 \\ -\mathbf{I}_3 & \mathbf{I}_3 \end{bmatrix} \quad (16)$$

where  $\mathbf{I}_3$  is the third rank identity matrix. The contribution of the truss members to the internal force vector is given by:

$$\mathbf{Q}_i = \sum_k^S N_k(\varepsilon_k) \cdot \mathbf{n}^T \quad (17)$$

The external force vector  $\mathbf{Q}_e$  contains the components of the external load acting on the system. All contributions are then assembled and the displacement vector is iteratively found by using the equation

$$\mathbf{u}_i = \mathbf{u}_{i-1} + (\mathbf{K}_m + \mathbf{K}_g)^{-1} (\mathbf{Q}_e - \mathbf{Q}_i) \quad (18)$$

starting from  $\mathbf{v}_0 = 0$ . The 2-norm of the residual  $\|\mathbf{Q}_e - \mathbf{Q}_i\|$  is used as convergence criterion. If the problem is applied to a linear elastic medium, the constitutive equation is

$$\sigma(\varepsilon_k) = E_k \cdot \frac{\Delta l_k}{l_{0k}} \quad (19)$$

Substituting (19) in Eqs. (15)–(17) gives

$$\mathbf{K}_m = K_k \cdot \mathbf{n}^T \mathbf{n} \quad (20)$$

$$\mathbf{K}_g = \frac{K_k}{l_k} \Delta l_k \begin{bmatrix} \mathbf{I}_3 & -\mathbf{I}_3 \\ -\mathbf{I}_3 & \mathbf{I}_3 \end{bmatrix} \quad (21)$$

$$\mathbf{Q}_i = K_k \Delta l_k \cdot \mathbf{n}^T \quad (22)$$

where  $E_k$  is the Young's modulus of the truss member,  $\mathbf{K}_k = A_k E_k / l_{0k}$  is its stiffness and  $\Delta l_k = \varepsilon_k l_{0k}$  is its elongation.

### 2.3. Numerical procedure

The numerical procedure used to solve the system of coupled non-linear equations in matrix form described above is based on the Newton-Raphson method. The algorithm must consider both the contribution of the elastic energy (relative to the deformation of the membrane) and of the adhesive energy (relative to its detachment at the interface). The former is calculated using the co-rotational formulation presented above; the latter is considered by adding to the tangential stiffness matrix  $\mathbf{K}$  the contributes given by the Jacobian matrix of the chosen traction-displacement law (Eq. (2)). To simulate the behavior of the membrane up to total delamination, displacement-control loading conditions are used. The discretization step  $\Delta u$  is controlled by an auxiliary algorithm which analyses the convergence speed of the process and varies  $\Delta u$  accordingly. The algorithm is implemented in C++. The Armadillo library (Sanderson and Curtin, 2016), OpenBLAS and LAPACK (Dongarra et al., 1993) are used for the linear algebra implementation. The algorithms provided by the superLU library (X. S. Li, 2005) are used to solve Eq. (18). The simulations are run on the OCCAM HPC cluster (Aldinucci et al., 2017).

### 3. Verification

Two known cases are considered to validate the numerical procedure: single tape peeling and axisymmetric peeling of a membrane.

#### 3.1. Tape single peeling

A single peeling test compatible with the hypotheses of Kendall's theory (Kendall, 1975) is considered. The peeling force can be written as

$$F = EL_y t \left[ \cos(\theta) - 1 + \sqrt{(1 - \cos(\theta))^2 + \frac{2\Delta\gamma}{tE}} \right] \quad (23)$$

where  $\Delta\gamma$  is the adhesive energy per unit area,  $\theta$  is the pulling angle,  $E$  is the Young's modulus of the tape and  $L_y$  and  $t$  are the width and the thickness of the tape respectively. The ratio  $R = \Delta\gamma / (tE)$  determines the two, "soft" or "rigid", tape regimes ( $R \gg 1$  or  $R \ll 1$ , respectively). Eq. (23) is valid adopting the approximation that the stress is concentrated at the peeling line, so that there is no elastic energy stored in the attached section of the tape.

In the case of the numerical model, if  $R \ll 1$  regions of the membrane far from the peeling line slip due to the elastic force that exceeds the adhesion force, so that the assumptions of Kendall's theory break down. This effect increases for smaller  $\theta$  angles.

As an example, we consider a membrane with the following geometric and mechanical parameters:  $L_x = 1$  mm,  $L_y = 8$  mm,  $t = 0.01$  mm,  $E = 1$  MPa. The membrane is discretized using square elements of side length  $l_0 = 0.1$  mm, imposing  $\nu = 0$  by removing the diagonal elements. Before delamination the tape is considered flat and fully adhered to the substrate. The adhesive energy is  $\Delta\gamma = 50$  kPa · mm, which is chosen in a relatively soft tape regime ( $R = 5$ ). This is consistent with previous papers in the literature (Heepe et al., 2017; Brely et al., 2018), including the original work by Kendall (Kendall, 1975). Fig. 2 shows the displacement field of a delaminating tape loaded by a peeling force. Numerical results for the peeling force vs the peeling angle, shown in Fig. 2, perfectly match those obtained using Eq. (23), thus validating the numerical code in this particular case.

Numerical results are obtained for different values of the characteristic length  $\delta$ . Discrepancies between the theoretical equation and the numerical data are observed in two cases: when  $\delta \lesssim 3l_0$  the resolution of the cohesive zone is insufficient in the mesh area where delamination is occurring, and oscillating values of the pull-off force are obtained. Instead, when  $\delta \gtrsim L/4$ , with  $L = \min(L_x, L_y)$ , the entire membrane delaminates and slides as soon as the load is applied, so that the maximal force is not reached and border effects prevail. To avoid these discrepancies between simulated and calculated results,  $\delta$  is chosen in all simulations so that  $5l_0 < \delta < L/5$ .

#### 3.2. Axisymmetric peeling

Another case which can be treated analytically, and is thus suitable for a comparison with numerical results, is the axisymmetric peeling of a membrane. This problem was treated in (Afferrante et al., 2013) in the case of an infinite membrane attached to a perfectly flat and infinitely rigid substrate. A vertical displacement  $u(r=0)$  is imposed at a single point, and the membrane starts to detach axisymmetrically, as shown in Fig. 3. Similarly to the single tape peeling problem described in the previous section, the analytical formulation holds if there is no deformation in the attached section of the tape. As demonstrated in (Afferrante et al., 2013), the force acting on the membrane is

$$F = 2\pi r t \cdot \frac{1}{2} E^* u'(r)^2 \cdot \sin\theta \quad (24)$$

where  $E^* = E/(1 - \nu^2)$ ,  $\theta$  is the peeling angle,  $u(r)$  is the vertical displacement of the membrane as a function of the radius  $r$  and  $u'(r) = \partial u / \partial r$ . Assuming small displacements,  $\sin\theta \simeq u'(r)$ , so that Eq. (24) can be rewritten as a differential equation:

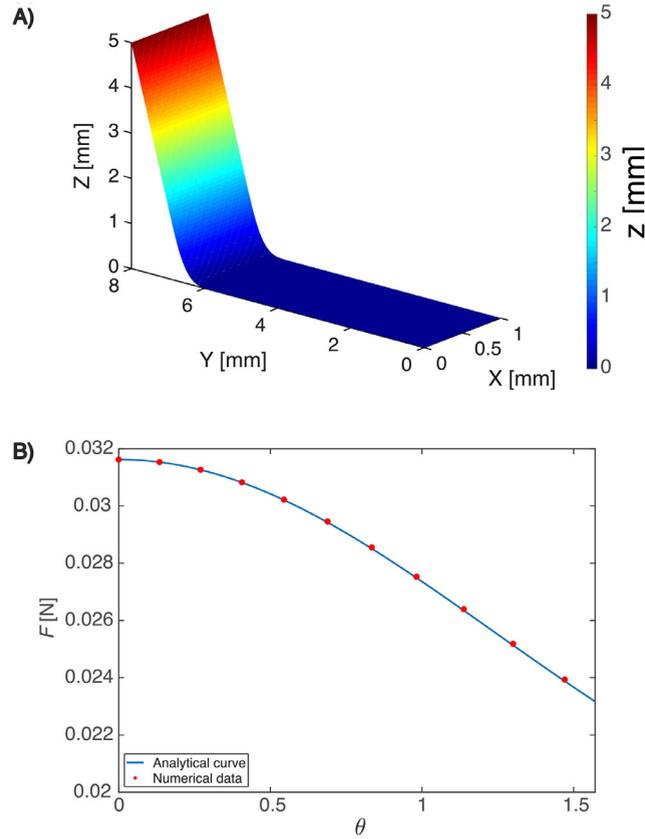


**Fig. 2.** Numerical simulation of single tape peeling (A) 3D displacement map. The colormap indicates the  $z$  displacement. (B) Numerical vs. analytical prediction of pull-off force vs peeling angle.

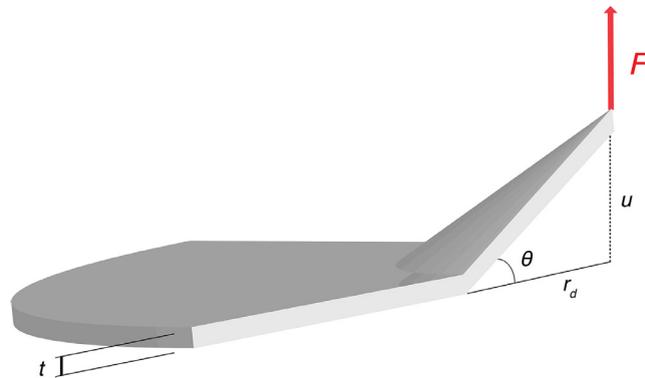


**Fig. 3.** Graphical representation of the axisymmetric peeling of a membrane (due to symmetry, only one quarter of the membrane is shown).

$$u'(r)^3 = \frac{F}{\pi t E^*} \cdot \frac{1}{r} \quad (25)$$

To solve this equation, the imposed displacement  $u(0) = u$  and the boundary condition  $u(r_d) = 0$  are enforced, where  $r_d$  is the detached radius. We thus obtain

$$u(r) = \frac{3}{2} \left( \frac{F}{E^* t \pi} \right)^{\frac{1}{3}} \left( r_d^{\frac{2}{3}} - r^{\frac{2}{3}} \right) \quad (26)$$

The load-displacement behavior of the system is thus:

$$F = \frac{8}{27} \pi t E^* \frac{u^3}{r_d^2} \quad (27)$$

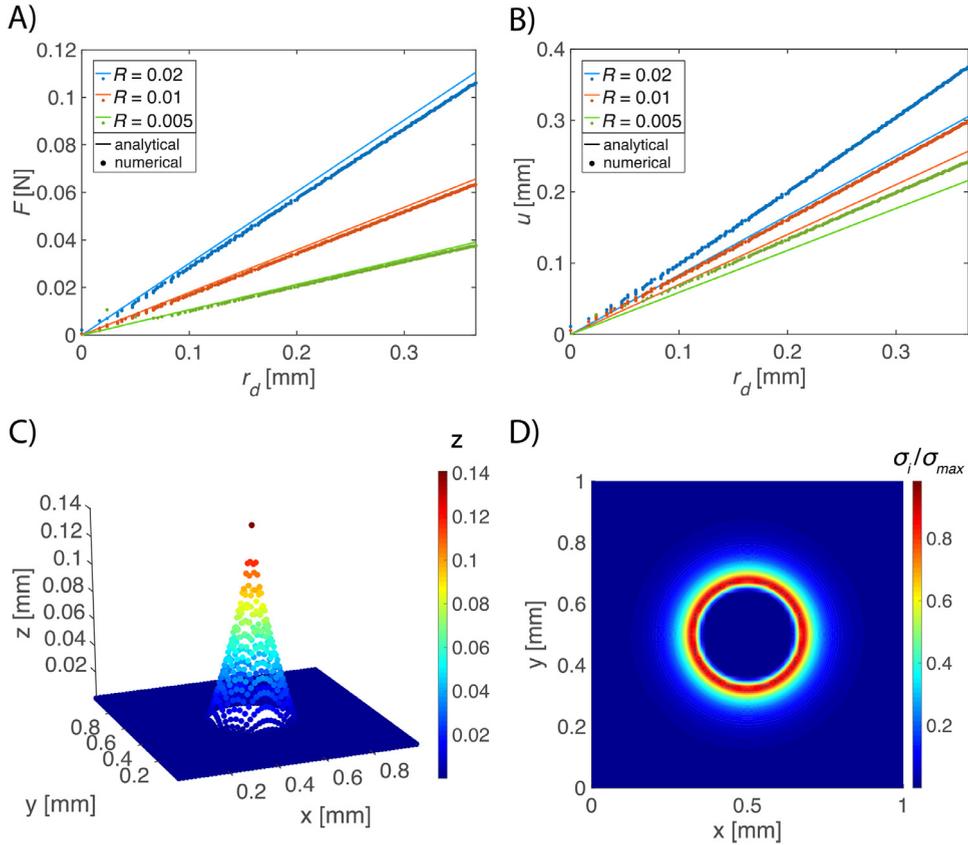


**Fig. 4.** Axisymmetric peeling of an elastic membrane. (A) peeling force vs radius of the detached area for different values of the nondimensional ratio  $R = \Delta\gamma/(Et)$ . The continuous lines are the analytical solutions found in (Afferrante et al., 2013), while dots represent the numerical result. (B) Imposed displacement vs radius of the detached area for different values of  $R$ , compared with the analytical solutions. (C) Membrane displacement map. The color map indicates the  $z$  displacement. (D) Normalized interface stress  $\sigma_i$  map.

This equation can be used to calculate the energy release rate of the system. The energy release rate is  $G = -\frac{1}{2\pi r_d} \left( \frac{\partial U}{\partial r_d} \right)_u$ , where  $U$  is the total elastic energy, which can be written as

$$U = \frac{1}{2E^*} \int \sigma^2 dV = \frac{2}{27} \frac{u^4}{r_d^2} E^* \pi t \tag{28}$$

where we used for the linear elastic stress-strain relation in the membrane  $\sigma_m = E^* \varepsilon_m \approx E^* \frac{1}{2} \left( \frac{du}{dr} \right)^2$ .  $G$  thus becomes:

$$G = 2 \frac{E^* t}{27} \frac{u^4}{r_d^4} \tag{29}$$

The energy balance criterion, i.e.  $\Delta\gamma = G$ , provides the critical force for delamination:

$$F \simeq \pi r_d (tE^*)^{\frac{1}{4}} \left( \frac{8}{3} \Delta\gamma \right)^{\frac{3}{4}} \tag{30}$$

where the radial displacement, the circumferential strain and the circumferential stress are assumed to be negligible.

Axisymmetric peeling is modelled numerically as follows. Simulations are performed for a membrane of  $L_x = L_y = 1$  mm,  $E = 0.5$  MPa,  $t = 1$   $\mu$ m,  $\nu = 1/3$ . Before load application, the membrane is considered flat and fully adhered to the substrate. Once loading and delamination begin, the detached radius  $r_d$  is measured at the point where the maximum delamination load occurs, i.e. it is chosen so that  $u(r_d) = \delta$ , where  $\delta$  is the characteristic length introduced in Eq. (3). Thus, from Eq. (4), the maximum interface stress  $\sigma_i$  is  $\sigma_{max} = \sigma_i(r = r_d)$ .

Fig. 4 shows the comparison between numerical and analytical results for the peeling force  $F$  and displacement  $u$  as a function of  $r_d$  for different values of the ratio  $R = \Delta\gamma/(Et)$ . Good agreement is found, with small discrepancies due to the simplified hypotheses of the analytical model, e.g. a rigid adhesive interface in the limit of small displacements, while in the numerical model, the interface is deformable and displacements can be large. The discrepancy between numerical and analytical results depends on two parameters:  $R$ , which determines the compliance of the system, and the characteristic

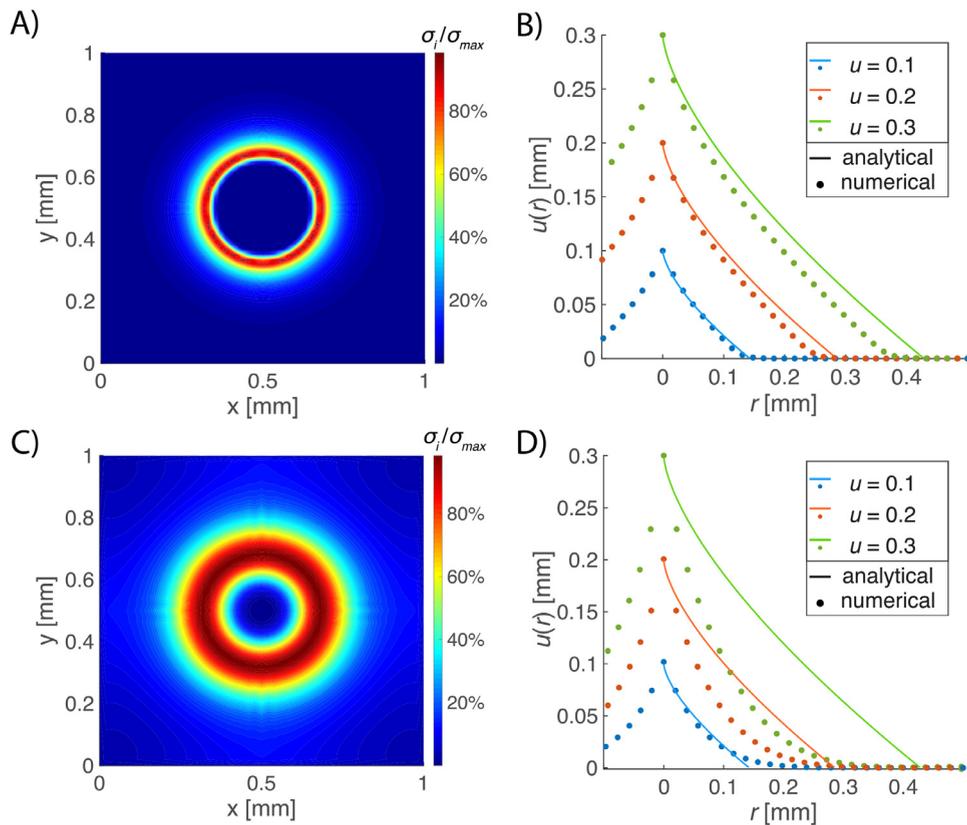


**Fig. 5.** Normalized interface stress maps and displacements for different values of  $R$  and  $\delta$ . (A) Normalized interface stress map for  $[R = 0.01, \delta = 0.01]$ . (B) Displacement for  $[R = 0.01, \delta = 0.01]$ . (C) Normalized interface stress map for  $[R = 0.1, \delta = 0.1]$ . (D) Displacement for  $[R = 0.1, \delta = 0.1]$ . Analytical results are compared with numerical simulations for different values of the imposed displacement  $u$ .

length  $\delta$ . Results in Fig. 4 are plotted for  $\delta = 0.01$  mm and  $R < 2 \cdot 10^{-2}$ . The peeling force increases approximately linearly with the displacement of the detached radius, as predicted by Eq. (30). This suggests that the force is directly proportional to the length of the peeling line, which is  $2\pi r_d$ . It can also be observed, as noted in (Afferrante et al., 2013), that the slope of the  $u$  vs  $r_d$  curve is constant for a given  $R$  (see Eq. (35)). Since  $\theta = \text{atan}(u/r_d)$ , this means that the peeling angle does not change during delamination, a result which is already found both in single peeling and symmetrical multiple peeling (Pugno and Gorb, 2009; Pugno, 2011; Brely et al., 2014).

To better understand the influence of  $R$  and  $\delta$ , in Fig. 5 we compare simulation results to analytical predictions (using Eq. (26)) for the displacement and stress distributions for  $[R = 0.01, \delta = 0.01]$  and  $[R = 0.1, \delta = 0.1]$ . When interface stresses are concentrated along the peeling line, as in Fig. 5A, there is good agreement between analytical and numerical profiles (Fig. 5B). On the other hand, for softer and more deformable structures, the stresses are distributed over a wider zone around the peeling line (Fig. 5C), which has two effects (Fig. 5D): first, this leads to a wider process zone, which involves the edges of the membrane from the onset of the pull-off phase, introducing edge effects that do not enable to reach the steady-state phase with constant  $\theta$ ; secondly, the deformation occurring in the delaminated part of the membrane displays a larger variation in  $\theta(r)$ , so that the calculated elongation of the membrane is larger than the simulated one. These two effects are responsible for the discrepancies between the theoretical and numerical results.

## 4. Results

The peeling behavior of an elastic membrane depends on numerous parameters: the dimensions of the membrane, including its aspect ratio, its Young's modulus, the adhesive energy of the interface, and the loading conditions, i.e. where and how the load is applied. A number of parametric studies are presented in this section to illustrate the model predictive capabilities and to gain insight into the overall behavior of an adhesive elastic membrane.

### 4.1. Pulling angle and adhesive directionality

We first investigate the effect of the pulling angle  $\theta$  on the pull-off force  $F$ . To do so, we simulate a flat membrane of size  $L_x = L_y = 1$  mm, thickness  $t = 1$   $\mu\text{m}$ , Young's modulus  $E = 0.5$  GPa, Poisson's ratio  $\nu = 1/3$ , adhesive energy  $\Delta\gamma =$

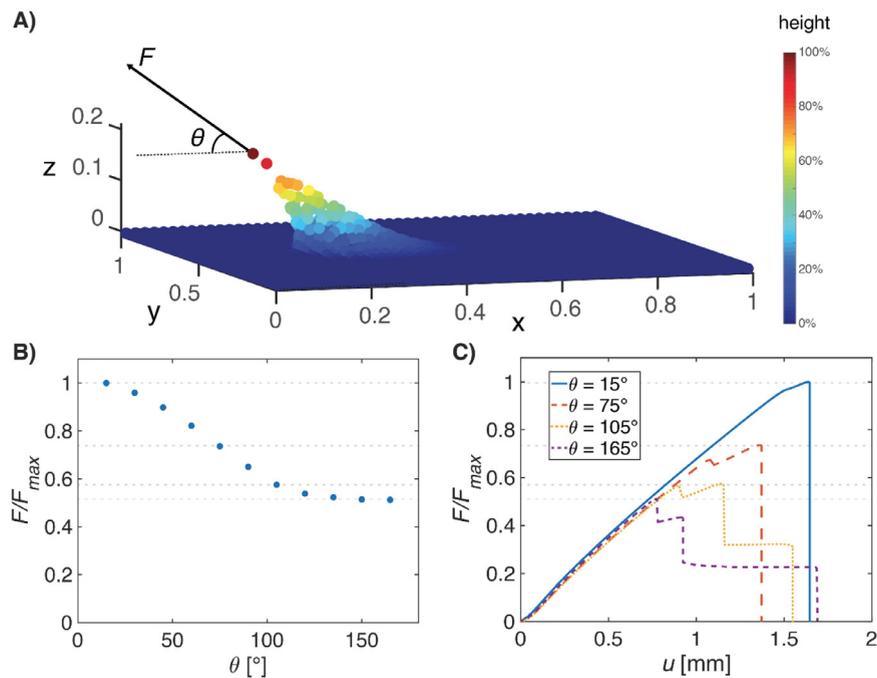


**Fig. 6.** (A) Schematic representation of the simulated asymmetric case. The membrane is pulled in a single off-center point by a force  $F$  directed at an angle  $\theta$ . (B) Normalized force vs pulling angle  $\theta$ . (C) Normalized force vs displacement for different values of the pulling angle  $\theta$ .

1 MPa · mm, initially fully in contact with the substrate. These are typical values for biological adhesive membranes such as, for example, spider disk attachments. The load is applied at a single point located at  $y = L_y/2$  (symmetric) and  $x = L_x/3$  (asymmetric). This configuration is schematically shown in Fig. 6A.

Fig. 6B shows the variation of the pull-off force (i.e. the maximum value of the load-displacement curve up to detachment) as a function of loading angle. The maximal pull-off force is obtained for  $\theta \approx 0^\circ$ , while the minimum is obtained in the opposite direction, for  $\theta \approx 180^\circ$ . There is greater variation of the load for small angles, i.e. greater load vs. angle sensitivity. This is due to the asymmetrical location of the pulling point with respect to the center of the membrane, which leads to an asymmetry in the available area for peeling, and therefore to the possibility of developing different peeling line lengths (and thus pull off forces) for different pulling angles. Thus, the membrane displays adhesive directionality and tunability, i.e. there is the possibility of modulating the adhesive force by varying the pulling direction. This is analogous to the Kendall single tape peeling case (The pull-off force also strongly depends on the location of the pulling point. If the membrane is pulled at its exact center, results for  $\theta = 0^\circ$  and  $\theta = 180^\circ$  coincide and the force-angle relationship is symmetrical). Fig. 6C shows the corresponding load-displacement relationship at four selected pulling angles, illustrating how the pull-off behavior changes also qualitatively as the angle increases. Each drop in the force coincides with the membrane peeling line reaching the border of the substrate.

We now focus on the behavior of the membrane during detachment to better understand how the membrane finite size influences the pull-off force, taking for example data obtained for  $\theta = 105^\circ$ . Fig. 7 shows the interface stress maps of the adhesive interface corresponding to the three force peaks and one of the force drops in the load-displacement plot (see related Videos 1, 2 in Supplementary informations). The stress distribution corresponding to the peak values indicates that a maximal adhesive force is obtained just before the delamination front reaches a membrane border. After this, a small displacement variation causes a “jump” of the delamination front which is associated to a sudden drop of the pulling force. When continuing to pull the membrane, the curve displays a continuous force increase until another border is reached. After each force drop, the curve increases with a smaller slope than previously.

A better analysis of the results shown in Fig. 6B is now possible. By looking at the different force-displacement curves we see that for  $\theta = 15^\circ$ , the delamination line reaches all borders almost simultaneously, whilst for  $\theta = 165^\circ$  the delamination line reaches the borders at a relatively small load, after which the delamination proceeds with a longer tape-like peeling process (at constant load). These behaviours are highlighted by looking at the displacement maps occurring during membrane delamination in the two cases, shown in Fig. 8. These plots demonstrate that the numerical model is able to simulate both concave and convex structures in the large displacement regime, which usually gives rise to ill-conditioned numerical problems.

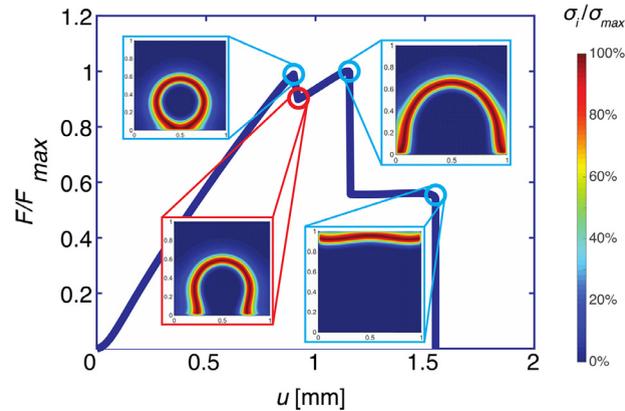


**Fig. 7.** Normalized force vs displacement for  $\theta = 105^\circ$ . Normalized interface stress  $\sigma_i$  maps highlighting the location of the delamination line in correspondence of some key points of the load-displacement curve. Dark blue indicates points where the interface is not subjected to any stress, which means that the membrane is totally attached or totally detached. Red areas represent points undergoing the maximal stress, i.e. the delamination front ( $u = \delta$ ,  $\sigma_i = \sigma_{max}$ ).

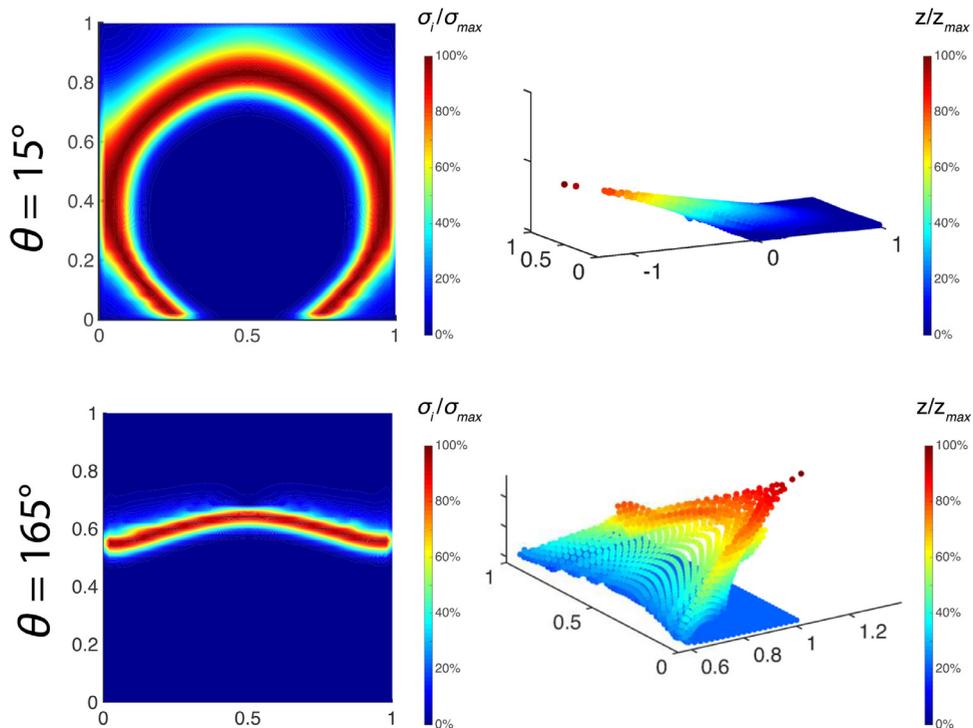


**Fig. 8.** Interface adhesive stress and membrane 3D displacement plot for two pulling angles at  $\theta = 15^\circ$  and  $\theta = 165^\circ$ . Data for  $\theta = 15^\circ$  is taken at the onset of delamination. Data for  $\theta = 165^\circ$  shows one of the time steps of the tape-like phase of the delamination. The peeling line, i.e. the length of the delamination front, is much larger in the first case than in the second one. Colours in the interface stress maps on the left show the normalized interface stress, while the color map in the 3D plots indicates the deformation along the vertical axis of the corresponding portion of the membrane.

#### 4.2. Dependence on the peeling line

To understand how the maximal adhesive force varies with geometrical parameters, it is necessary to determine a correlation between the pull-off force and a global physical quantity. One possibility is to consider the total delaminated area. However, this parameter can be ruled out by looking at Fig. 7, where the delaminated area is constantly growing while the force does not vary monotonically. Another possibility is to consider the total peeling line, i.e. the length of the delamination front, which varies non-monotonically during the delamination phase. Results from analysis of the data reported in Fig. 6 are shown in Fig. 9, where the peeling force is compared to the peeling line length at various points during delamination. The two quantities show a good level of correlation, proving that for a membrane with given mechanical properties, different

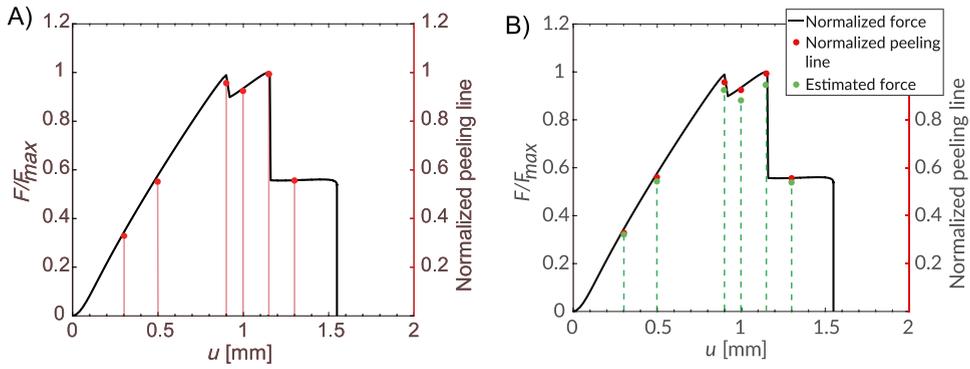


**Fig. 9.** Normalized force and normalized total peeling line length vs displacement for an elastic membrane pulled at an angle of  $\theta = 105^\circ$ . The two observables display a very good correlation, proving that the length of the delamination front is the main physical quantity which determines the pull-off force during detachment. The green points represent the estimated forces using Eq. (33).

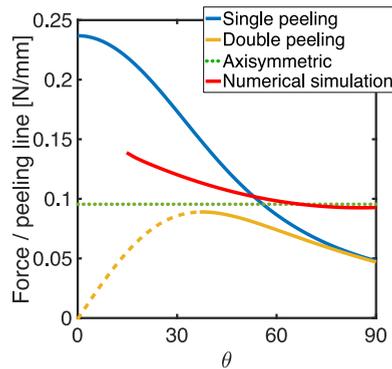


**Fig. 10.** Force per unit peeling line vs. pulling angle  $\theta$  for the three considered cases: membrane delamination, single peeling and double peeling. In the double peeling case,  $\theta$  is the angle between the tape and the substrate (the “peeling angle”). The dashed part of the curve represents nonphysical values, corresponding to negative initial peeling angles (Pugno, 2011; Brely et al., 2014). The dotted line represents estimated force using Eq. (33).

loading conditions and different geometrical properties affect the shape of the delamination front, whose length in turn determines the pull-off force. This is true at least in cases, such as the present one, in which the stresses are concentrated around the peeling line and peeling angles do not deviate significantly from  $90^\circ$ .

To determine the proportionality constant between the pull-off force and the peeling line, we compare the numerically calculated force per unit peeling line  $\hat{f}_M$  vs. the peeling angle  $\theta$  obtained in the single and double peeling cases. We compare the forces for  $\theta \in [0^\circ, 90^\circ]$ .  $\hat{f}_M$  is symmetrical for  $\theta \in [90^\circ, 180^\circ]$ . In the double peeling case, the tape is pulled normally to the surface and  $\theta$  is the peeling angle instead of the angle of the pulling force. For single peeling, Eq. (23) can be rewritten as (Kendall, 1975):

$$\hat{f}_{SP} = Et \left[ \cos(\theta) - 1 + \sqrt{(1 - \cos(\theta))^2 + 2R} \right] \quad (31)$$

The pull-off force in a double peeling problem can be obtained by using multiple peeling theory (Pugno, 2011). The force necessary to peel a v-shaped tape is given by the superposition of the two single tape peeling occurring in the structure. If the v-shape is symmetrical, it follows that the pull-off force acting on each tape is  $F_{SP} \sin \theta$ , and thus:

$$\hat{f}_{DP} = \sin(\theta) Et \left[ \cos(\theta) - 1 + \sqrt{(1 - \cos(\theta))^2 + 2R} \right] \quad (32)$$

Results are shown in Fig. 10. It is clear that contrary to the single and double peeling cases, the peeling angle of the membrane is not constant along the whole length of the peeling line. This leads to a variation in the normalized pull-off force, which is found to be intermediate between the single and double peeling cases for small and intermediate angles. Interestingly, for these parameters and peeling angles close to  $90^\circ$ ,  $\hat{f}_M$  exceeds the value for the single and double peeling cases, indicating that this configuration realizes a sort of optimum.  $\hat{f}_M$  appears to be weakly dependent on  $\theta$ : we thus compare its values to the analytical prediction for the axisymmetric delamination of a membrane (Eq. (30)), which can

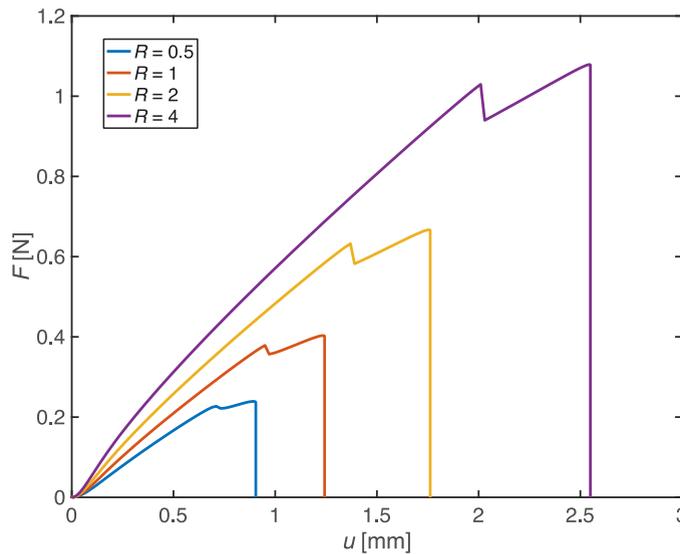


Fig. 11. Force vs displacement for different values of  $R$ .

provide a theoretical estimation of the peeling line proportionality:

$$\hat{F}_{AX} = \frac{1}{2} \left( \frac{tE}{1-\nu^2} \right)^{\frac{1}{4}} \left( \frac{8}{3} \Delta\gamma \right)^{\frac{3}{4}} \quad (33)$$

where  $\hat{F}_{AX}$  is the force in Eq. (30) divided by the peeling length  $2\pi r_d$ . Results are shown in Fig. 10. Clearly, this estimation improves as the pulling angle approaches  $90^\circ$ . In most cases, the discrepancy is small, as can be seen comparing the calculated curve and the estimated force values in Fig. 9.

#### 4.3. Dependence on adhesive energy

The adhesive energy, i.e. work of adhesion, is an important mechanical parameter in any adhesion problem. As shown in Eq. (30), the analytical solution of the axisymmetrical peeling force for an infinite membrane is dependent on the adhesive energy  $\Delta\gamma$ . In particular, by using the ratio  $R$ , Eq. (30) can be rewritten as:

$$F = \pi r_d t E^* \left( \frac{8}{3} R \right)^{\frac{3}{4}} \quad (34)$$

while the related displacement (Afferrante et al., 2013) can be obtained by equating Eq. (27) and Eq. (30) as:

$$u = r_d \cdot \left( \frac{27}{2} R \right)^{\frac{1}{4}} \quad (35)$$

The dependence of the pull-off force  $F$  on  $R$  has been discussed in contact splitting problems (Arzt et al., 2003) and in multiple peeling problems (Pugno, 2011; Brely et al., 2014). The behavior of an adhesive elastic membrane is now studied for different values of the parameter  $R$  for  $\theta = 90^\circ$ . Results are shown in Fig. 11. Looking at the force-displacement relationship for different values of  $R$ , it can be seen that both the “strength” (i.e. the maximal force), and the “extensibility” (i.e. the maximal displacement), increase with  $R$ , but the overall qualitative behavior is unchanged. The dependence is non-linear and displays a proportionality of  $F \propto R^{0.73}$ , in accordance with Eq. (34), while the extensibility scales as  $R^{0.47}$ , similar to the predicted value of  $\frac{1}{4}$  in Eq. (35).

#### 4.4. Dependence on membrane aspect ratio

Different loading conditions and mechanical properties have a considerable influence on the adhesive behavior of the membrane. We now investigate the dependence on the geometrical properties for different pulling angles. To do so, an elastic membrane of area  $A = 1 \text{ mm}^2$  is pulled at  $\theta = 45^\circ, 90^\circ, 135^\circ$  for a force application point located at  $L_x/3$  and  $L_y/2$ . The adhesive energy is  $\Delta\gamma = 50 \text{ MPa} \cdot \text{mm}$ . Simulations are performed for different aspect ratios  $L_y/L_x$ . Results are shown in Fig. 12.

The pull-off force is strongly dependent on both aspect ratio and loading angle. For a given angle, the pull-off force is maximum for specific aspect ratio values (Fig. 12A). For a normal force ( $90^\circ$ ), two optimal ratios are found when the membrane is slightly larger in width than in length, or vice versa ( $L_x \approx 0.75 L_y, L_y \approx 0.75 L_x$ ). If the membrane is too wide or

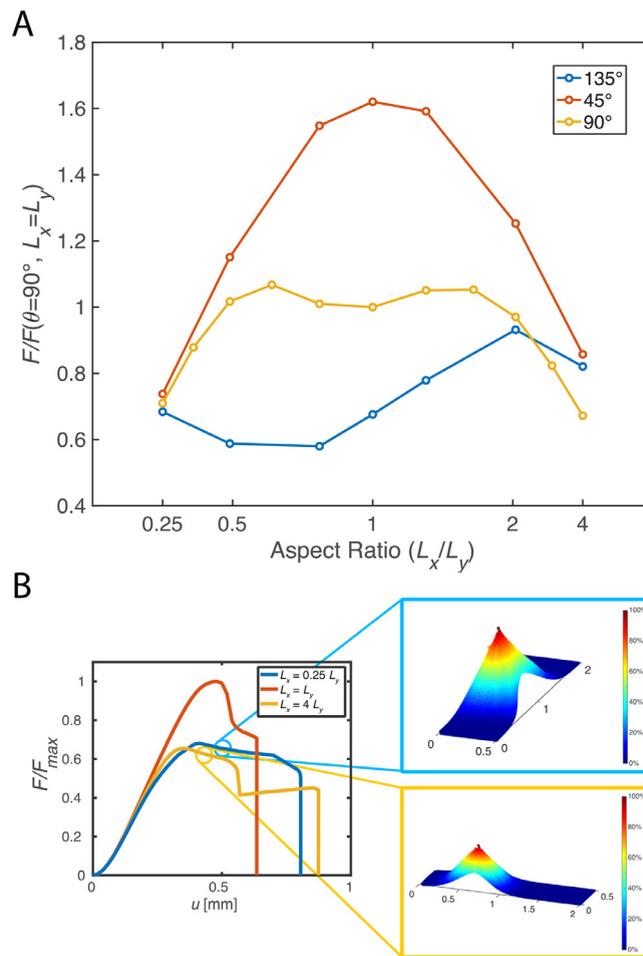


**Fig. 12.** (A) Normalized pull-off force vs the aspect ratio of the membrane for three pulling angles. (B) Normalized force vs displacement for three aspect ratios and  $\theta = 90^\circ$ . A 3D displacement plot of the membrane is shown for  $L_x = 0.25 L_y$  and  $L_x = 4 L_y$  at the delamination stages corresponding to the indicated points. The color maps indicate the deformations along the vertical axes. A similar behavior occurs for corresponding double peeling geometries.

too long, the adhesive force quickly drops down to values  $\approx 25\%$  lower than the maximal value for a ratio of  $L_y/L_x = 0.5$  and  $\approx 35\%$  lower for  $L_y/L_x = 2$ . This can again be explained by analysing the force-displacement curves (Fig. 12B): when the membrane is too wide or too narrow, the two edges that delaminate first are the front and rear ones, or the two lateral ones, respectively. When this happens, a double peeling phase starts: the force remains relatively constant until total delamination occurs ( $L_x = 0.25 L_y$ ) or one of the two ends completely detaches and a single peeling phase begins ( $L_x = 4 L_y$ ). A similar behavior is also observed for  $\theta = 45^\circ$ , but the maximal pull-off force is obtained for an aspect ratio equal to 1. For high pulling angles such as  $\theta = 135^\circ$  the membrane starts a single peeling phase at an early stage. In this case, the pull-off force is only dependent from the width of the tape, so larger pull-off forces are reached for wider membranes.

## 5. Conclusions

In this work, we have presented a new theoretical-numerical model capable of simulating the delamination of elastic membranes attached to a substrate. With the model it is possible to derive total pull-off forces, full 3D displacements and stresses acting on the membrane for oblique pulling forces applied at any point, including in cases when convex regions and ripples develop on the surface. Results have been compared with those obtained by single peeling theory and axisymmetric peeling theory, leading to a validation of the model. The dependence on mechanical and geometrical parameters, such as the ratio  $R$ , the peeling line length or the pulling angle, has been highlighted, showing how these are the main factors determining the pull-off force. Moreover, it has been proven that for a membrane of given mechanical characteristics, there is a direct correlation between the pull-off force and the length of the delamination front, i.e. the peeling line. This implies that to maximize the pull-off forces and global adhesion, the membrane should be designed in such a way as to maximize how the peeling line (i.e. the maximum stress distributions deriving from membrane deformation) exploit the entire available adhesive area. This can provide inspiration for the design of structured surfaces that allow to exploit this concept for optimized adhesion or anti-adhesion.

This approach can be applied to the study of complex problems with heterogeneous membranes, non-trivial geometries, or patterned surfaces. Further improvements to the model could lead to a better understanding of open mechanical problems in or beyond adhesion. Simulations can be extended to include friction phenomena, using different cohesive laws and interface models, or even fracture phenomena, describing the opening and sliding of a crack interface. Moreover, the versatility of the approach could be exploited to analyze specific biological or bio-inspired problems, such as mussel attachment systems, mushroom-like punches in bioinspired adhesives or octopus suction cups. More complex membrane constitutive laws, including plasticity or stiffening behavior, can be easily implemented, thus enabling the reliable simulation of advanced adhesive problems, where the interplay between geometry, structure, material heterogeneity and mechanical constitutive behavior can lead to unexpected and possibly extreme properties.

## Acknowledgements

FB is supported by the FET Proactive “Neurofibres” grant No. 732344, the COST Action CA15216 “European Network of Bioadhesion Expertise”, by Progetto d’Ateneo/Fondazione San Paolo “Metapp”, n. CSTO160004, and by the Italian Ministry of Education, University and Research (MIUR) under the “Departments of Excellence” grant L.232/2016. NMP is supported by the European Commission under the Graphene Flagship Core 2 Grant no. 785219 (WP14 “Composites”) and FET Proactive “Neurofibres” Grant no. 732344 as well as by the Italian Ministry of Education, University and Research (MIUR) under the “Departments of Excellence” Grant L.232/2016, the ARS01-01384-PROSCAN Grant and the PRIN-20177TTP3S Grant. Computational resources were provided by the Centro di Competenza sul Calcolo Scientifico (C3S) of the University of Torino (c3s.unito.it).

## References

- Absi, E., Prager, W., 1975. A comparison of equivalence and finite element methods. *Comput. Methods Appl. Mech. Eng.* 6 (1), 59–64. doi:10.1016/0045-7825(75)90015-8.
- Afferrante, L., Carbone, G., Demelio, G., Pugno, N.M., 2013. Adhesion of elastic thin films: double peeling of tapes versus axisymmetric peeling of membranes. *Tribol. Lett.* 52 (3), 439–447. doi:10.1007/s11249-013-0227-6.
- Aldinucci, M., Bagnasco, S., Lusso, S., Pasteris, P., Rabellino, S., Vallero, S., 2017. OCCAM: A flexible, multi-purpose and extendable HPC cluster. *J. Phys. Conf. Ser.* 898 (8), 082039–082047.
- Arzt, E., Gorb, S.N., Spolenak, R., 2003. From micro to nano contacts in biological attachment devices. *Proc. Nat. Acad. Sci.* 100 (19), 10603–10606. doi:10.1073/pnas.1534701100.
- Barenblatt, G.I., 1962. The mathematical theory of equilibrium cracks in brittle fracture. *Adv Appl Mech* 7 (C), 55–129. doi:10.1016/S0065-2156(08)70121-2.
- Bhushan, B., 2007. Adhesion of multi-level hierarchical attachment systems in Gecko feet. *J. Adhes. Sci. Technol.* 21 (12–13), 1213–1258. doi:10.1163/156856107782328353.
- Brely, L., Bosia, F., Pugno, N.M., 2014. Numerical implementation of multiple peeling theory and its application to spider web anchorages. *Interface Focus* 5 (1), 1–9. doi:10.1098/rsfs.2014.0051.
- Brely, L., Bosia, F., Pugno, N.M., 2015. A hierarchical lattice spring model to simulate the mechanics of 2-D materials-based composites. *Front. Mater.* 2 (51), doi:10.3389/fmats.2015.00051.
- Brely, L., Bosia, F., Pugno, N.M., 2018a. Emergence of the interplay between hierarchy and contact splitting in biological adhesion highlighted through a hierarchical shear lag model. *Soft Matter* 14 (26), 5509–5518. doi:10.1039/C8SM00507A.
- Brely, L., Bosia, F., Pugno, N.M., 2018b. The influence of substrate roughness, patterning, curvature, and compliance in peeling problems. *Bioinspir. Biomim.* 13 (2), 026004. doi:10.1088/1748-3190/aaa0e5.
- Brodoceanu, D., Bauer, C.T., Kroner, E., Arzt, E., Kraus, T., 2016. Hierarchical bioinspired adhesive surfaces—a review. *Bioinspir. Biomim.* 11 (5), 051001. doi:10.1088/1748-3190/11/5/051001.
- Carbone, G., Pierro, E., Gorb, S.N., 2011. Origin of the superior adhesive performance of mushroom-shaped microstructured surfaces. *Soft Matter* 7 (12), 5545. doi:10.1039/c0sm01482f.
- Cerda, E., Mahadevan, L., 2003. Geometry and physics of wrinkling. *Phys. Rev. Lett.* 90 (7), 074302. doi:10.1103/PhysRevLett.90.074302.
- Chen, B., Wu, P., Gao, H., 2009. Pre-Tension generates strongly reversible adhesion of a spatula pad on substrate. *J. Royal Soc. Interface* 6 (35), 529–537. doi:10.1098/rsif.2008.0322.
- Chen, H., Lin, E., Jiao, Y., Liu, Y., 2014. A generalized 2D non-local lattice spring model for fracture simulation. *Comput. Mech.* 54 (6), 1541–1558. doi:10.1007/s00466-014-1075-4.
- Costagliola, G., Bosia, F., Pugno, N.M., 2018. A 2-D model for friction of complex anisotropic surfaces. *J. Mech. Phys. Solids.* 112, 50–65. doi:10.1016/j.jmps.2017.11.015.
- Crocombe, A.D., Adams, R.D., 1981. Peel analysis using the finite element method. *J. Adhes.* 12 (2), 127–139. doi:10.1080/00218468108071194.
- Cutkosky, M.R., 2015. Climbing with adhesion: from bioinspiration to biounderstanding. *Interface Focus* 5, 20150015. doi:10.1098/rsfs.2015.0015.
- Daltorio, K.A., Horschler, A.D., Gorb, S.N., Ritzmann, R.E., Quinn, R.D., 2005. A small wall-walking robot with compliant, adhesive feet. In: 2005 IEEE/RSJ International Conference on Intelligent Robots and Systems. IEEE, pp. 3648–3653. doi:10.1109/IROS.2005.1545596.
- Das, S., Cadirov, N., Chary, S., Kaufman, Y., Hogan, J., Turner, Kimberly L., Israelachvili, J.N., 2015. Stick-Slip friction of Gecko-mimetic flaps on smooth and rough surfaces. *J. Royal Soc. Interface* 12 (104), doi:10.1098/rsif.2014.1346, 20141346–20141346.
- Derjaguin, B.V., Muller, V.M., Toporov, Y.P., 1975. Effect of contact deformation on the adhesion of elastic solids. *J. Colloidal Interface Sci.* 53 (2), 314–326. [http://linkinghub.elsevier.com/retrieve/pii/0021979775900181%0Apapers3://publication/doi/10.1016/0021-9797\(75\)90018-1](http://linkinghub.elsevier.com/retrieve/pii/0021979775900181%0Apapers3://publication/doi/10.1016/0021-9797(75)90018-1).
- Dimaki, A.V., Dmitriev, A.I., Menga, N., Papangelo, A., Ciavarella, M., Popov, Valentin L., 2016. Fast high-resolution simulation of the gross slip wear of axially symmetric contacts. *Tribol. Trans.* 59 (1), 189–194. doi:10.1080/10402004.2015.1065529.
- Dimitri, R., Trullo, M., De Lorenzis, L., Zavarise, G., 2015. Coupled cohesive zone models for mixed-mode fracture: a comparative study. *Eng. Fract. Mech.* 148, 145–179. doi:10.1016/j.engfracmech.2015.09.029.
- Dongarra, J., Pozo, R., Walker, D., 1993. LAPACK++: A Design Overview of Object-Oriented Extensions for High Performance Linear Algebra. In: *Proceedings of the Supercomputing '93 Meeting, Portland, Oregon, November 15–19*, pp. 162–171.
- Dugdale, D.S., 1960. Yielding of steel sheets containing slits. *J. Mech. Phys. Solids* 8 (2), 100–104. doi:10.1016/0022-5096(60)90013-2.
- Grawe, I., Wolff, J.O., Gorb, S.N., 2014. Composition and substrate-dependent strength of the silken attachment discs in spiders. *J. Royal Soc. Interface* 11 (98), doi:10.1098/rsif.2014.0477, 20140477–20140477.
- Hrennikoff, A., 1941. Solution of problems of elasticity by the framework method. *J. Appl. Mech.* 8 (4), 169–175.
- Hu, S., Jiang, H., Xia, Z., Gao, X., 2010. Friction and Adhesion of Hierarchical Carbon Nanotube Structures for Biomimetic Dry Adhesives: Multiscale Modeling. *ACS Appl. Mater. Interfaces* 2 (9), 2570–2578. doi:10.1021/am100409s.

- Johnson, K.L., Kendall, K., Roberts, A.D., 1971. Surface energy and the contact of elastic solids. *Proc. Royal Soc. A* 324 (1558), 301–313. doi:[10.1098/rspa.1971.0141](https://doi.org/10.1098/rspa.1971.0141).
- Kendall, K., 1975. Thin-Film peeling-the elastic term. *J. Phys. D* 8 (13), 1449–1452. doi:[10.1088/0022-3727/8/13/005](https://doi.org/10.1088/0022-3727/8/13/005).
- Kim, S., Spenko, M., Trujillo, S., Heyneman, B., Santos, D., Cutkosky, M.R., 2008. Smooth vertical surface climbing with directional adhesion. *IEEE Trans. Robot.* 24 (1), 65–74. doi:[10.1109/TRO.2007.909786](https://doi.org/10.1109/TRO.2007.909786).
- Labonte, D., Federle, W., 2016. Biomechanics of shear-sensitive adhesion in climbing animals: peeling, pre-tension and sliding-induced changes in interface strength. *J. Royal Soc. Interface* 13 (122). doi:[10.1098/rsif.2016.0373](https://doi.org/10.1098/rsif.2016.0373).
- Lai, Y., Gao, X., Zhuang, H., Huang, J., Lin, C., Jiang, L., 2009. Designing superhydrophobic porous nanostructures with tunable water adhesion. *Adv. Mater.* 21 (37), 3799–3803. doi:[10.1002/adma.200900686](https://doi.org/10.1002/adma.200900686).
- Heepe, L., Hue, L., Gorb, S.N., 2017. Bio-Inspired structured adhesives. In: Heepe, L., Xue, L., Gorb, S.N. (Eds.). *Biologically-Inspired Systems*, 9. Springer International Publishing, Cham doi:[10.1007/978-3-319-59114-8](https://doi.org/10.1007/978-3-319-59114-8).
- Leonard, B.D., Sadeghi, F., Shinde, S., Mittelbach, M., 2012. A numerical and experimental investigation of fretting wear and a new procedure for fretting wear maps. *Tribol. Trans.* 313–324. doi:[10.1080/10402004.2012.654598](https://doi.org/10.1080/10402004.2012.654598).
- Li, X.S., 2005. An overview of SuperLU. *ACM Trans. Math. Softw.* 31 (3), 302–325.
- Limkatanyu, S., Prachasaree, W., Kaewkulchai, G., Kwon, M., 2013. Total lagrangian formulation of 2D bar element using vectorial kinematical description. *KSCSE J. Civil Eng.* 17 (6), 1348–1358. doi:[10.1007/s12205-013-0424-8](https://doi.org/10.1007/s12205-013-0424-8).
- Maugis, D., 1992. Adhesion of spheres: the JKR-DMT transition using a Dugdale model. *J. Colloid Interface Sci* 150 (1), 243–269. doi:[10.1016/0021-9797\(92\)90285-T](https://doi.org/10.1016/0021-9797(92)90285-T).
- McGarry, J.P., Máirtín, É., Parry, G., Beltz, Glenn E., 2014. Potential-Based and non-potential-based cohesive zone formulations under mixed-mode separation and over-closure. part I: theoretical analysis. *J. Mech. Phys. Solids* 63 (1), 336–362. doi:[10.1016/j.jmps.2013.08.020](https://doi.org/10.1016/j.jmps.2013.08.020).
- Mo, X., Wu, Y., Zhang, J., Hang, T., Li, M., 2015. Bioinspired multifunctional Au nanostructures with switchable adhesion. *Langmuir* 31 (39), 10850–10858. doi:[10.1021/acs.langmuir.5b02472](https://doi.org/10.1021/acs.langmuir.5b02472).
- Nishino, F., Ikeda, K., Sakurai, T., Hasegawa, A., 1984. A total lagrangian nonlinear analysis of elastic trusses. *Doboku Gakkai Ronbunshu* 1 (344), 39–53. doi:[10.2208/jscej.1984.39](https://doi.org/10.2208/jscej.1984.39).
- Nukala, Phani Kumar V.V., Zapperi, S., Āimunović, S., 2005. Statistical properties of fracture in a random spring model. *Phys. Rev. E* 71 (6 Pt. 2), 066106. doi:[10.1103/PhysRevE.71.066106](https://doi.org/10.1103/PhysRevE.71.066106).
- Ostoja-Starzewski, M., 2002. Lattice models in micromechanics. *Appl. Mech. Rev.* 55 (1), 35. doi:[10.1115/1.1432990](https://doi.org/10.1115/1.1432990).
- Palacio, Manuel L.B., Bhushan, B., 2012. Bioadhesion: A review of concepts and applications. *Philos. Tran. Royal Soci. A* 370 (1967), 2321–2347. doi:[10.1098/rsta.2011.0483](https://doi.org/10.1098/rsta.2011.0483).
- Park, K., Paulino, Glaucio H., 2013. Cohesive zone models: a critical review of traction-separation relationships across fracture surfaces. *Appl. Mech. Rev.* 64 (6), 060802. doi:[10.1115/1.4023110](https://doi.org/10.1115/1.4023110).
- Pohrt, R., Popov, Valentin L., 2015. Adhesive contact simulation of elastic solids using local mesh-dependent detachment criterion in boundary elements method. *Facta Univ., Ser. 13* (1), 3–10.
- Prokopovich, P., Starov, V., 2011. Adhesion models: from single to multiple asperity contacts. *Adv. Colloid Interface Sci.* 168 (1–2), 210–222. doi:[10.1016/j.cis.2011.03.004](https://doi.org/10.1016/j.cis.2011.03.004).
- Pugno, N.M., 2011. The theory of multiple peeling. *Int. J. Fract.* 171 (2), 185–193. doi:[10.1007/s10704-011-9638-2](https://doi.org/10.1007/s10704-011-9638-2).
- Pugno, N.M., Gorb, S.N., 2009. Functional mechanism of biological adhesive systems described by multiple peeling approach: a new angle for optimal adhesion. In: *Proceedings of the 12th International Conference on Fracture 2009 (ICF-12)*, pp. 1–9.
- Pugno, N.M., Lepore, E., 2008. Observation of optimal Gecko's adhesion on nanorough surfaces. *Biosystems* 94 (3), 218–222. doi:[10.1016/j.biosystems.2008.06.009](https://doi.org/10.1016/j.biosystems.2008.06.009).
- Rakshit, S., Sivasankar, S., 2014. Biomechanics of cell adhesion: how force regulates the lifetime of adhesive bonds at the single molecule level. *Phys. Chem. Chem. Phys.* 16, 2211–2223. doi:[10.1039/c3cp53963f](https://doi.org/10.1039/c3cp53963f).
- Rey, V., Anciaux, G., Molinari, J.F., 2017. Normal adhesive contact on rough surfaces: efficient algorithm for FFT-Based BEM resolution. *Comput. Mech.* 60 (1), 69–81. doi:[10.1007/s00466-017-1392-5](https://doi.org/10.1007/s00466-017-1392-5).
- Rice, J.R., Wang, J.-S., 1989. Embrittlement of interfaces by solute segregation. *Mater. Sci. Eng.* 107, 23–40. doi:[10.1016/0921-5093\(89\)90372-9](https://doi.org/10.1016/0921-5093(89)90372-9).
- Salehani, M.K., Irani, N., Müser, M.H., Nicola, L., 2018. Modeling coupled normal and tangential tractions in adhesive contacts. *Tribol. Int.* 124 (March), 93–101. doi:[10.1016/j.triboint.2018.03.022](https://doi.org/10.1016/j.triboint.2018.03.022).
- Salehani, M. K., Irani, N., 2018. "A coupled mixed-mode cohesive zone model: an extension to three-dimensional contact problems." <http://arxiv.org/abs/1801.03430>.
- Sanderson, C., Curtin, R., 2016. Armadillo: a template-based C++ library for linear algebra. *J. Open Source Softw.* 1 (2), 26.
- Sauer, R.A., 2016. A survey of computational models for adhesion. *J. Adhes.* 92 (2), 81–120. doi:[10.1080/00218464.2014.1003210](https://doi.org/10.1080/00218464.2014.1003210).
- Savkoor, A.R., Briggs, G.A.D., 1977. Effect of tangential force on the contact of elastic solids in adhesion. *Proc. R. Soc. London Ser A* 356 (1684), 103–114. doi:[10.1098/rspa.1977.0123](https://doi.org/10.1098/rspa.1977.0123).
- Shen, L., Jagota, A., Hui, C.Y., 2009. Mechanism of sliding friction on a film-terminated fibrillar interface. *Langmuir* 25 (5), 2772–2780. doi:[10.1021/la803390x](https://doi.org/10.1021/la803390x).
- Thouless, M.D., Yang, Q.D., 2008. A parametric study of the peel test. *Int. J. Adhes. Adhes.* 28 (4–5), 176–184. doi:[10.1016/j.ijadhadh.2007.06.006](https://doi.org/10.1016/j.ijadhadh.2007.06.006).
- Tian, Y., Pesika, N., Zeng, H., Rosenberg, K., Zhao, B., McGuiggan, P., Autumn, K., Israelachvili, J., 2006. Adhesion and friction in Gecko toe attachment and detachment. *Proc. Nat. Acad. Sci.* 103 (51), 19320–19325. doi:[10.1073/pnas.0608841103](https://doi.org/10.1073/pnas.0608841103).
- Vakis, A.I., Yastrebov, V.A., Scheibert, J., Nicola, L., Dini, D., Minfray, C., Almqvist, A., et al., 2018. Modeling and simulation in tribology across scales: an overview. *Tribology International* 125, 169–199. doi:[10.1016/j.triboint.2018.02.005](https://doi.org/10.1016/j.triboint.2018.02.005).
- Valoroso, N., Champaney, L., 2006. A damage-mechanics-based approach for modeling decohesion in adhesively bonded assemblies. *Eng. Fract. Mech.* 73 (18), 2774–2801. doi:[10.1016/j.engfracmech.2006.04.029](https://doi.org/10.1016/j.engfracmech.2006.04.029).
- Warrior, N.A., Pickett, A.K., Lourenco, N.S.F., 2003. Mixed-Mode delamination - Experimental and numerical studies. *Strain* 39 (4), 153–159. doi:[10.1046/j.1475-1305.2003.00088.x](https://doi.org/10.1046/j.1475-1305.2003.00088.x).
- Wolff, J.O., Gorb, S.N., 2016. Attachment structures and adhesive secretions in arachnids. *Biologically-Inspired Systems*, 7. Springer International Publishing, Cham doi:[10.1007/978-3-319-45713-0](https://doi.org/10.1007/978-3-319-45713-0).
- Xu, X.P., Needleman, A., 1994. Numerical simulations of fast crack growth in brittle solids. *J. Mech. Phys. Solids* 42 (9), 1397–1434. doi:[10.1016/0022-5096\(94\)90003-5](https://doi.org/10.1016/0022-5096(94)90003-5).
- Yastrebov, V.A., Durand, J., Proudhon, H., Cailletaud, G., 2011. Rough surface contact analysis by means of the finite element method and of a new reduced model. *Comptes Rendus - Mécanique* 339 (7–8), 473–490. doi:[10.1016/j.crme.2011.05.006](https://doi.org/10.1016/j.crme.2011.05.006).
- Yaw, L. 2009. "2D Co-Rotational truss formulation," [https://gab.wallawalla.edu/~louie.yaw/Co-rotational\\_docs/2Dcorot\\_truss.pdf](https://gab.wallawalla.edu/~louie.yaw/Co-rotational_docs/2Dcorot_truss.pdf).
- Zhang, Z., Paulino, G.H., 2005. Cohesive zone modeling of dynamic failure in homogeneous and functionally graded materials. *International Journal of Plasticity* 21, 1195–1254. doi:[10.1016/j.jiplas.2004.06.009](https://doi.org/10.1016/j.jiplas.2004.06.009).